J Mater Sci (2006) 41:4420–4433
DOI 10.1007/s10853-006-0154-0

Spherical-aberration correction in tandem with the restoration of the exit-plane wavefunction: synergetic tools for the imaging of lattice imperfections in crystalline solids at atomic resolution

Karsten Tillmann · Lothar Houben · Andreas Thust · Knut Urban

Received: 22 December 2005 / Accepted: 14 February 2006 / Published online: 30 June 2006

Abstract With the availability of resolution-boosting and delocalization-minimizing techniques, aberration-corrected high-resolution transmission electron microscopy is currently enjoying great popularity with respect to the atomic scale imaging of lattice imperfections in crystalline solid-state materials. In the present review, the most striking practical benefits arising from the synergetic combination of two sophisticated state-of-the-art techniques, i.e. spherical-aberration-corrected imaging as well as the numerical restoration of the exit-plane wavefunction from a focal series of high-resolution micrographs, are illustrated by highlighting their combined use for the atomic-scale characterization of misfit dislocations, stacking faults and grain boundaries in common semiconductor materials and metastable metal phases. For these purposes recent progress is reviewed in the atomic-scale characterization of (i) Lomer-type misfit dislocations at $In_xGa_{1-x}As/GaAs$ heterointerfaces and extrinsic stacking fault ribbons in GaAs together with the associated lattice displacements [Tillmann et al. (2004) Microsc Microanal 10:185], (ii) the core structure of chromium implantation-induced Frank partial dislocations in GaN [Tillmann et al. (2005) Microsc Microanal 11:534] as well as (iii) tilt boundaries between β-phase Ta crystallites in thin metallization layers [Tillmann et al. (2006) Phil Mag, in press]. In addition, practical advantages are demonstrated of the retrieval of the exit-plane wavefunction not only for the measurement and subsequent elimination of residual lens aberrations still present in aberration-corrected microscopy, but also for the proper alignment of specimens during operation of the electron microscope.

K. Tillmann (✉) · L. Houben · A. Thust · K. Urban
Ernst Ruska-Centre for Microscopy and Spectroscopy with Electrons and Institute of Solid State Research, Research Centre Jülich, D-52425 Jülich, Germany
e-mail: k.tillmann@fz-juelich.de

Introduction

From a materials science point of view, of particular interest for high-resolution transmission electron microscopy is at present (i) the pursuit of sub-ångström resolution at medium acceleration voltages [4–6] also associated with (ii) the straightforward interpretability of image contrast features encoded in experimental micrographs [7–9] characterized by (iii) a rather low image delocalization in the vicinity of lattice imperfections [10, 11]. Two sophisticated techniques for accomplishing all three of these objectives simultaneously, which were previously not incapable of being implemented during operation of ''traditional'' medium-voltage instruments equipped with field emission gun emitters and operated under high-resolution conditions, have attracted much interest in recent years.

Double hexapole corrector elements as originally proposed by Rose [12] enabling a compensation of detrimental lens aberrations can now be applied in practice in standard instruments operated at medium voltages [13, 14]. As a result, the electron microscope can be operated as a variable spherical-aberration instrument where the aberration coefficient C_S emerges as an additional parameter for extending the point resolution under phase contrast imaging conditions to the instrumental information limit together with the simultaneous maximization of phase contrast and the minimization of contrast delocalization [15]. When employing a negative C_S value combined with

a certain overfocus setting $Z_{opt} > 0$, not only a substantial contrast improvement is achieved but low-nuclear charge elements can also be imaged at bright atom contrast features in the vicinity of high-nuclear charge atoms [7, 8].

Moreover, numerical restoration techniques enable the restoration of the exit-plane wavefunction from a focal series [16–18] of micrographs. By this means, all spatial information up to the instrumental information limit can be retrieved, also allowing for a subsequent elimination of residual lens aberrations still present in aberration-corrected microscopy [19, 20]. Additionally, the on-line retrieval of the exit-plane wavefunction during operation of the microscope was demonstrated as a suitable tool for precise sample alignment when analysing the symmetry properties of ''local'' diffraction patterns evaluated from the complex-valued exit-plane wavefunction.

The present compilation of materials science applications reviews recent progress in the characterization of lattice defects at atomic resolution and for the quantification of atom column positions in the vicinity of lattice imperfections arising from the specific combination of both the above-mentioned state-of-the-art techniques. Special emphasis will be given to synergy effects enabling the identification of specific atom columns at dislocation cores and grain boundaries, thus providing information on the validity of certain dislocation core and interface structure models in GaAs- and GaN-based nanostructures and Ta polycrystallites, respectively. Experimental analysis techniques include both the use a spherical aberration-corrected 200 kV instrument together with the numerical retrieval of the exit-plane wavefunction from a through-focus series of experimental micrographs.

High-resolution imaging at a corrector tuning towards negative C_S values

When the electron microscope is operated as a variable spherical-aberration corrected instrument, the aberration coefficient C_S emerges as an additional parameter for the tuning of the transfer characteristics of the instrument. Consequently, when setting the constant of spherical aberration to an optimized value

$$C_S = -64/27\ \lambda^{-3} g_{max}^{-4} \tag{1}$$

and choosing an overfocus setting of the objective lens

$$Z_{opt} = 16/9\ \lambda^{-1} g_{max}^{-2} \tag{2}$$

with λ and $1/g_{max}$, denoting the electron wavelength and information limit of the instrument, respectively, a high amount of negative phase contrast, which is a synonym for bright atom contrast conditions, may be achieved simultaneously with a largely minimized image delocalization describing the ''blurring'' of object points in the image plane [8, 15]. This set-up of the instrument thus yields directly interpretable high-resolution micrographs accompanied by a residual image delocalization in the imaging plane of

$$R = 16/27\ g_{max}^{-1}. \tag{3}$$

With this tuning, Z_{opt} replaces the Scherzer condition of ''traditional'' high-resolution microscopy and the partially coherent phase contrast transfer function as displayed in Fig. 1 is extended up to the information limit $1/g_{max}$ of the instrument. Simplifying the imaging process to a linear theory, a weak phase object is then imaged under bright atom contrast conditions [21]. A substantial contrast improvement is achieved since the linear phase contrast and the non-linear dark field signal add rather than subtract, as is usual when applying ''traditional'' high-resolution imaging modes [22]. In the strict sense Eqs. (1)–(3) base upon a first order expansion of the aberration function, thus neglecting any detrimental impact of higher order lens aberrations. As the hexapole corrector of the CM-200 FEG ST allows for a sufficient correction of aberrations up to the third order and higher order aberrations will become relevant not until $1/g_{max}$ becomes smaller than 100 pm [23, 24], these aberrations do not need to be considered for the instrument under consideration.

Using an aberration-corrected CM-200 FEG ST microscope, the above-mentioned parameter settings yield Z_{opt} = 11.6 nm, C_S = – 40.6 μm and R = 0.08 nm when set to an electron wavelength of λ = 2.51 pm and an information limit of $1/g_{max}$ = 0.125 nm with the latter value measured from a Young's fringe analysis [15].

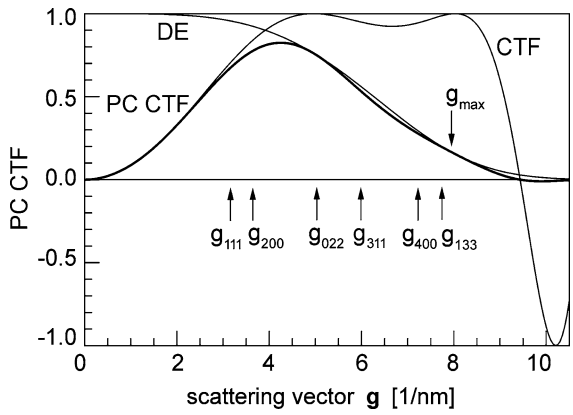

Fig. 1 Partially coherent contrast transfer function (thicker black line) based on parameters λ = 2.51 pm, C_S = −40.6 μm, Z = 11.6 nm together with 0.2 mrad for the semi-angle of beam convergence and 6.4 nm for the half-width of the Gaussian spread of defocus. Arrows indicate crystalline reflections in GaAs

Benefits from the restoration of the exit-plane wavefunction

Apart from the advantages arising from negative spherical aberration-corrected imaging, the additional numerical restoration of the exit-plane wavefunction $\Psi(\mathbf{r})$ from a through focus series of micrographs basically offers five further improvements.

First, $\Psi(\mathbf{r})$ is in principle free from non-linear imaging artefacts, and by the combination of many images taken at different defocus values the insufficient contrast transfer of low spatial frequencies, caused by employing a rather small C_S value during recording of single micrographs taken under optimized conditions, is reduced considerably. Secondly, by extracting information from about 10–20 images, the signal-to-noise ratio at high spatial frequencies can be substantially increased compared to a single Z_{opt} micrograph [25]. Thirdly, even the application of small C_S values, which is a prerequisite for obtaining phase contrast, induces a parasitic delocalization R whereas the numerically retrieved $\Psi(\mathbf{r})$ is ideally free from any delocalization-induced artefacts.

Fourthly, the availability of the complex-valued quantity $\Psi(\mathbf{r})$ allows for the numerical *a posterior* measurement of residual lens aberrations. This aspect is of special practical importance as experiments show that not all aberrations of the microscope are sufficiently constant over the period of operation or else cannot be determined before the experiment with sufficient accuracy. In detail, the measurement of even aberrations, i.e. the defocus Z and the twofold astigmatism A_1, may be carried out by processing the weak signal originating from amorphous overlayers [19] while the procedures for determining odd aberrations, i.e. the axial coma B_2 and the threefold astigmatism A_3, are based on the analysis of the degree of symmetry with respect to crystalline features visible in the phase $\Phi(\mathbf{r})$ and amplitude $A(\mathbf{r})$ images of the exit-plane wavefunction [20].

Fifthly, the numerical restoration of $\Psi(\mathbf{r})$ makes it possible to calculate ''local'' diffraction patterns from specimen areas as small as desired. If evaluated during operation of the microscope, the judgement of the symmetry properties of these ''local'' diffraction patterns is a most convenient tool for the proper orientation of specimen areas under investigation with an accuracy well below 3 mrad while the vast majority of high-resolution micrographs taken from samples aligned by ''traditional'' specimen alignment procedures demonstrate off-zone-axis orientations well above 10 mrads [1].

Negative C_S imaging performed in tandem with the restoration of the exit-plane wavefunction

The measurement of minor crystal misorientations with respect to the incident electron beam and the quantification of the magnitude and, if applicable, direction of residual lens aberrations including absolute focus values by means of the retrieval of the exit-plane wavefunction brings about a dramatic reduction of the search area of imaging parameters when performing numerical image calculations. The availability of corresponding ''known unknowns'' was demonstrated to be indeed an auxiliary tool for the commensurability of complete focal series of calculated images of GaAs(110) with corresponding experimental micrographs. By this means it was possible to reproduce the entirety of the contrast feature asymmetries, mainly caused by residual axial coma and three-fold astigmatism, in good agreement with experimental data [1].

To clarify the common fallacy that the above-mentioned benefits associated with the numerical retrieval of the exit-plane wavefunction do not necessitate the use of spherical aberration-corrected instrumentation it is emphasized that, if measurements are to be performed in a timely manner, the numerical *a posterior* measurement of residual lens aberrations requires a sufficient pre-reduction of the very same aberrations.

Moreover, image delocalization in a non-corrected instrument will generally not be less than [10]

$$R_L = C_S/4\ \lambda^3 g_{max}^3 \tag{4}$$

and will only be within reach at Lichte's defocus of least confusion

$$Z_L = -3/4 C_S \lambda^2 g_{max}^2 \tag{5}$$

which, unfortunately, is associated with the great disadvantage that the phase contrast transfer function exhibits a large number of rapid contrast oscillations at medium spatial frequencies, and the corresponding contrast reversals make the resulting image quite difficult to interpret. The very same image delocalization does not only have a detrimental effect on the spread out of structural information in the vicinity of internal boundaries and lattice defects, but also on the acquisition of information at marginal areas of the recording medium. Thus, the rather large R_L values associated with an uncorrected instrument represent a serious limitation for the usable field of view of the detector, e.g. a charge-coupled device (CCD) camera. Clearly, not even sophisticated numerical techniques will permit the retrieval of the entire intrinsic specimen structure when structural information has spread to the outside of the CCD detector and, thus, cannot be recorded.

Experimental setup

The electron micrographs presented here were recorded with a Philips CM-200 FEG instrument equipped with a

computer-controlled electromagnetic hexapole system to compensate the spherical aberration of the objective lens [26]. Prior to recording micrographs of the specimen regions of interest, an optical coarse adjustment of the electron microscope's hexapole corrector elements was performed by analysing Zemlin tableaus taken from amorphous specimen areas with an incident electron beam tilted up to 20 mrad from the optical axis [27] thus yielding an initial estimate of the quality of higher-order aberration corrections. Laying down an optimized negative spherical aberration $C_S = -40$ μm, see above, the magnitudes of residual aberration coefficients were limited to $A_1 \leq 2.0$ nm for the twofold astigmatism, $A_2 \leq 170$ nm for the threefold astigmatism and $B_2 \leq 55$ nm for the axial coma [26]. Focal series of about 10–20 images were recorded using a 1×1 k charge-coupled device camera system choosing magnification settings which ensured a sampling rate of about 20 pm per picture element, i.e. an image discretization well below the Nyquist frequency with respect to half of the information limit $1/(2\ g_{max}) = 0.065$ nm of the electron microscope.

Materials science application: extrinsic stacking faults in GaAs(110)

Both of the microscopic analysis techniques described in the preceding sections have been applied to a fairly wide range of defect structure problems arising in solid state research. In the following sections, we highlight their combined use by discussing materials science applications related to specific cases.

As a first application, we shall focus on extrinsic stacking faults in GaAs(110) formed upon the dissociation of 60° dislocations with Burgers vectors of type $\mathbf{b} = a/2 <110>$ with $a = 0.5653$ nm denoting the lattice parameter of the material. These 60° dislocations are referred to as perfect dislocations since the Burgers vector corresponds to the smallest primitive lattice vector in the sphalerite structure [28] and, when the dislocation line direction is parallel to the crystallographic $[1\bar{1}0]$ direction, then Burgers vectors $a/2\ [0\bar{1}1]$ and $a/2\ [\bar{1}0\bar{1}]$ both form a 60° angle with the dislocation line. Perfect 60 °dislocations may dissociate into two partial dislocations bounding either an intrinsic or an extrinsic stacking fault ribbon [29]. Assuming a dislocation line along the crystallographic $[1\bar{1}0]$ direction, the Burgers vector dissociation reaction is:

$$a/2[0\bar{1}1] \rightarrow a/6[1\bar{2}1] + a/6[\bar{1}\bar{1}2] \quad (6)$$

with the Burgers vectors of both partials inclining angles of 30° and 90° with the dislocation line, respectively. It is only recently that great efforts have been made to investigate the core structure of 30° and 90° partials, both theoretically applying *ab initio* calculations [30–32] and experimentally employing advanced electron microscopy techniques, also including the numerical retrieval of the exit-plane wavefunction [33, 34].

Figure 2 (a) displays the Z_{opt} micrograph $I(\mathbf{r})$ of the terminating zone of an extrinsic stacking fault in GaAs viewed along the crystallographic $[1\bar{1}0]$ direction. Afar the double stacking fault ribbon, the micrograph demonstrates clearly separated contrast dots at spacings of $a/4 \approx 0.14$ nm forming atomic dumbbells. However, four conspicuous deficiencies and contrast artefacts become evident from close inspection of the micrograph.

Firstly, although the atom columns are clearly resolved, spurious intensity peaks unrelated to the structure are observed in between the atom column positions. These spurious intensity peaks are due to a transfer of low spatial frequencies at severe phase offsets, especially of the strongly excited {111} beam amplitudes [22].

Secondly, a kidney-shaped distortion of the dumbbells perpendicular to the polar [001] direction is observed. As can be shown from quantitative measurements on the associated ''local'' diffraction pattern evaluated from the retrieved exit-plane wavefunction, these distortions are not due to any potential misorientation of the sample but instead result from residual lens aberrations amounting to $A_1 = 2.2$ nm (83°), $B_2 = 110$ nm (83°), and $A_2 = 150$ nm (43°) with the values in parentheses indicating the respective azimuth angles inclined with the [001] direction [1]. For that reason, the phase $\Phi_{unc}(\mathbf{r})$ of exit-plane wavefunction, as displayed at higher magnification in Fig. 3, still shows comparable distortions of the contrast dumbbells as long as these residual aberrations are not compensated during the initial step of the reconstruction process. By contrast, the final phase image $\Phi(\mathbf{r})$ is free of any distortions after the aberrations A_i and B_i mentioned above have been eliminated.

Thirdly, a minor smear of the atom column related contrast dots to elongated tenons in the upper right image area of Fig. 2(a) indicates that these regions are slightly out of optimum focus, which is most probably due to the wedge-shaped geometry of the sample.

Fourthly, the dumbbells of the double stacking fault ribbon are not resolved in the Z_{opt} micrograph, which may be due either to the residual image delocalization, mechanical instabilities, or a genuine structural effect.

In contrast, the retrieved phase $\Phi(\mathbf{r})$ and amplitude $A(\mathbf{r})$ images displayed in Fig. 2b and c, respectively, allow an accurate identification of the atomic arrangement of the double stacking fault ribbon and, especially, the core structure of the dislocation terminating the defect. Additionally, the spurious contrast peaks in between the atom column positions visible in the experimental $I(\mathbf{r})$ image are resolved in the phase image $\Phi(\mathbf{r})$ as the exit-plane wavefunction is not hampered by contrast transfer

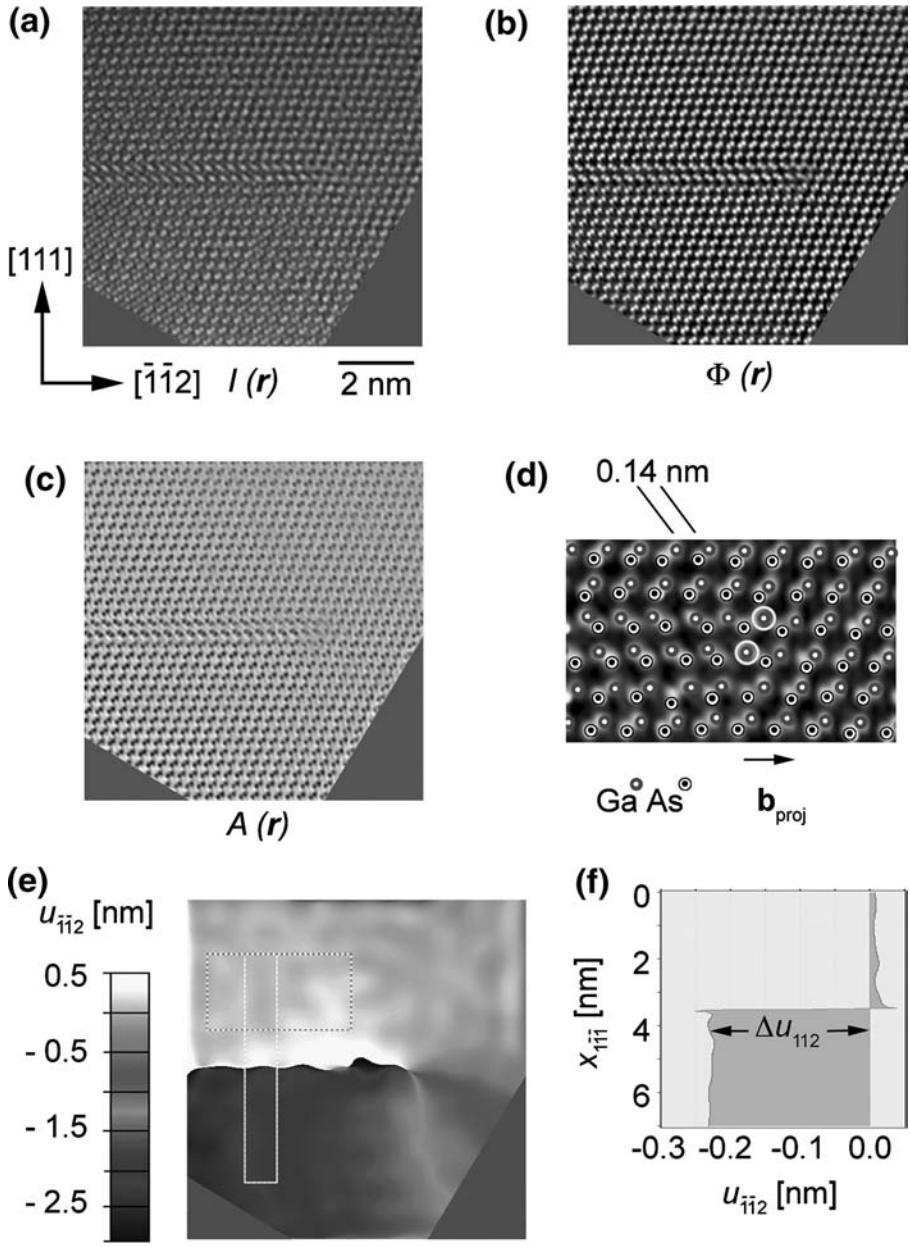

Fig. 2 Extrinsic stacking fault ribbon in GaAs laterally bound by a 90° partial dislocation with $\mathbf{b}_{proj} = a/6[\bar{1}\bar{1}2]$. (**a**) Optimum focus micrograph $I(\mathbf{r})$ taken along the $[1\bar{1}0]$ zone axis orientation of the sample. (**b**) Restored phase image $\Phi(\mathbf{r})$ and (**c**) amplitude image $A(\mathbf{r})$ evaluated from the associated through-focus series of micrographs. (**d**) Magnified clipping of $\Phi(\mathbf{r})$ with the positions of atom columns superimposed and the dislocation core positions of two 30° sub-partials indicated by lighter grey circles. (**e**) Contour representation of the lattice displacements $u_{\bar{1}\bar{1}2}(\mathbf{r})$ measured along the $[\bar{1}\bar{1}2]$ direction with reference to the area framed by a dashed line as evaluated from the phase image. (**f**) Displacement profile measured perpendicular to the double stacking fault ribbon at the area indicated by the lighter grey frame

limitations of the instrument's objective lens. Furthermore, the phase image is richer in contrast compared to the single micrograph $I(\mathbf{r})$ as there are no limitations with respect to temporal and spatial coherence. The retrieved phase information, moreover, benefits from the averaging of information from a complete series of micrographs, which enhances the signal-to-noise ratio compared to a single micrograph taken under Z_{opt} defocusing conditions.

When applying geometrical phase analysis algorithms [35] to measure the elastic displacement component $\Delta u_{\bar{1}\bar{1}2}$ along the crystallographic $[\bar{1}\bar{1}2]$ direction, i.e. along the direction of the stacking fault double ribbon, a $\Delta u_{\bar{1}\bar{1}2}(\mathbf{r})$ distribution according to Fig. 2e is obtained from the $\Phi(\mathbf{r})$ image. The contour representation of elastic displacements reveals strong gradients ambient to the dislocation core as well as two mainly undistorted lattices, which are

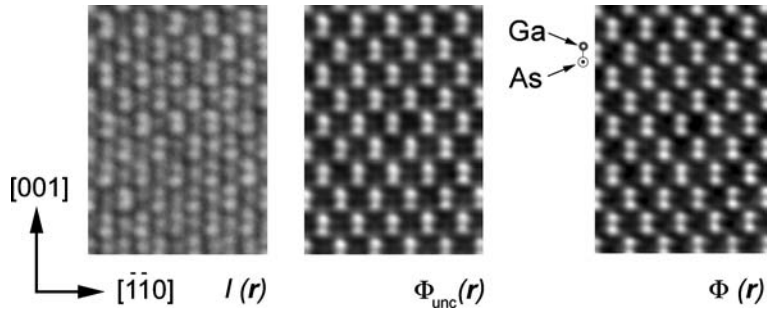

Fig. 3 Illustration of the impact of contrast transfer and parasitic lens aberrations on image contrast features. Optimum focus micrograph $I(\mathbf{r})$ of the GaAs taken along the $[1\bar{1}0]$ zone axis orientation of the sample together with the associated phase images $\Phi_{\mathrm{unc}}(\mathbf{r})$ and $\Phi(\mathbf{r})$ of the exit-plane wavefunction obtained when respectively neglecting and considering residual lens aberrations amounting to A_1 = 2.2 nm (83°), B_2 = 110 nm (83°), and A_2 = 150 nm (43°) with the values in parentheses indicating the respective azimuth angles inclined with the [001] direction

homogeneously shifted against each other at the left-sided image regions. Fig. 2f displays a line profile $u_{\bar{1}\bar{1}2}(\mathbf{r}_{\bar{1}\bar{1}\bar{1}})$ extracted from the displacement distribution along the $[\bar{1}\bar{1}\bar{1}]$ direction. The associated position of the line profile is indicated in the figure by the lighter grey rectangle. The profile shows two conspicuous plateaus separated by an abrupt discontinuity of $\Delta u_{\bar{1}\bar{1}2}$ = 0.234 nm 0.06 nm. This quantity is in excellent agreement with the closing vector associated with a 90° partial dislocation terminating an extrinsic stacking fault, for which a total shift of lattice planes of $\Delta u_{\bar{1}\bar{1}2,30^\circ} = 2\, b_{\mathrm{proj},90^\circ} = a/6[\bar{1}\bar{1}2] = 0.231$ nm is expected [29].

When also measuring the polarity of the sample, for instance by the evaluation of a set of relevant reciprocal-space amplitudes from the complex exit-plane wavefunction and the subsequent trimming of simulated data [1], individual bright contrast dots in the $\Phi(\mathbf{r})$ image may be directly associated either with gallium or arsenic columns. Corresponding atomic species are superimposed onto the magnified clipping of the phase image displayed in Fig. 2d. As can be seen from this figure, the 90° partial is itself composed of two sub-partials, whose core positions are indicated by the lighter grey circles. As the associated columns lie on narrowly spaced (111) lattice planes, the sub-partials are of the glide set type. Both cores are made up of gallium columns leading to a so-called β dislocation [36]. Moreover, the figure also reveals a symmetrical sixfold structure of the overall dislocation core, which is in perfect agreement with a 90° partial composed of two 30° partials separated by two atomic layers and terminating an extrinsic stacking fault [29].

Going a step further, local variations in the distortion of the atomic dumbbells across the stacking fault double ribbon may also be measured at some distance from the dislocation core. Corresponding procedures reveal an antisymmetric torsion and dilatation of atomic dumbbells with respect to the faulted double ribbon, which is found to decrease with distance from the stacking fault. This observation may be explained by the terminating sub-partial biasing the rearrangement of atom columns in the vicinity of the stacking fault ribbons and by next but one neighbour interactions between different atomic species [2].

Materials science application: interfacial edge dislocations in InGaAs/GaAs(110)

Apart from the dissociation of 60° dislocation as considered in the previous section, two appropriately oriented 60° dislocations may also undergo a reaction to form a pure edge dislocation with $\mathbf{b} = a/2$ [110] at a $1\bar{1}0$ line direction, i.e. with a Burgers vector perpendicular to the dislocation line. These edge dislocations are referred to as Lomer dislocations [37] and may relieve the strain energy in lattice mismatched epitaxial layer systems grown along the [001] direction most efficiently as they are perfectly aligned with the principal in-plane direction of mismatch-induced elastic strains. In view of the multiplicity of conceivable lattice positions of the slide-in half plane's terminal point numerous core structure models have been proposed for these types of dislocations [38, 39].

Figure 4 displays a set of images including an optimum focus micrograph $I(\mathbf{r})$ together with the correspondingly restored amplitude $A(\mathbf{r})$ and phase $\Phi(\mathbf{r})$ data of a Lomer dislocation with $\mathbf{b} = a/2$ $\bar{1}\bar{1}0$ formed in the proximity of the interface between the $In_{0.3}Ga_{0.7}As$ epilayer and the GaAs(001) substrate viewed with a $1\bar{1}0$ zone axis orientation of the sample. As discussed in the preceding section, spurious contrast peaks in between the column positions and the kidney-shaped distortions of the clearly resolved GaAs dumbbells are due to convoluted contrast transfer and residual lens aberrations, respectively.

The essential benefit of the combined use of the numerical retrieval of the exit-plane wavefunction with aberration-corrected imaging again becomes evident if the atomic structure of the dislocation core is considered in more detail. This structure is basically not resolved in the

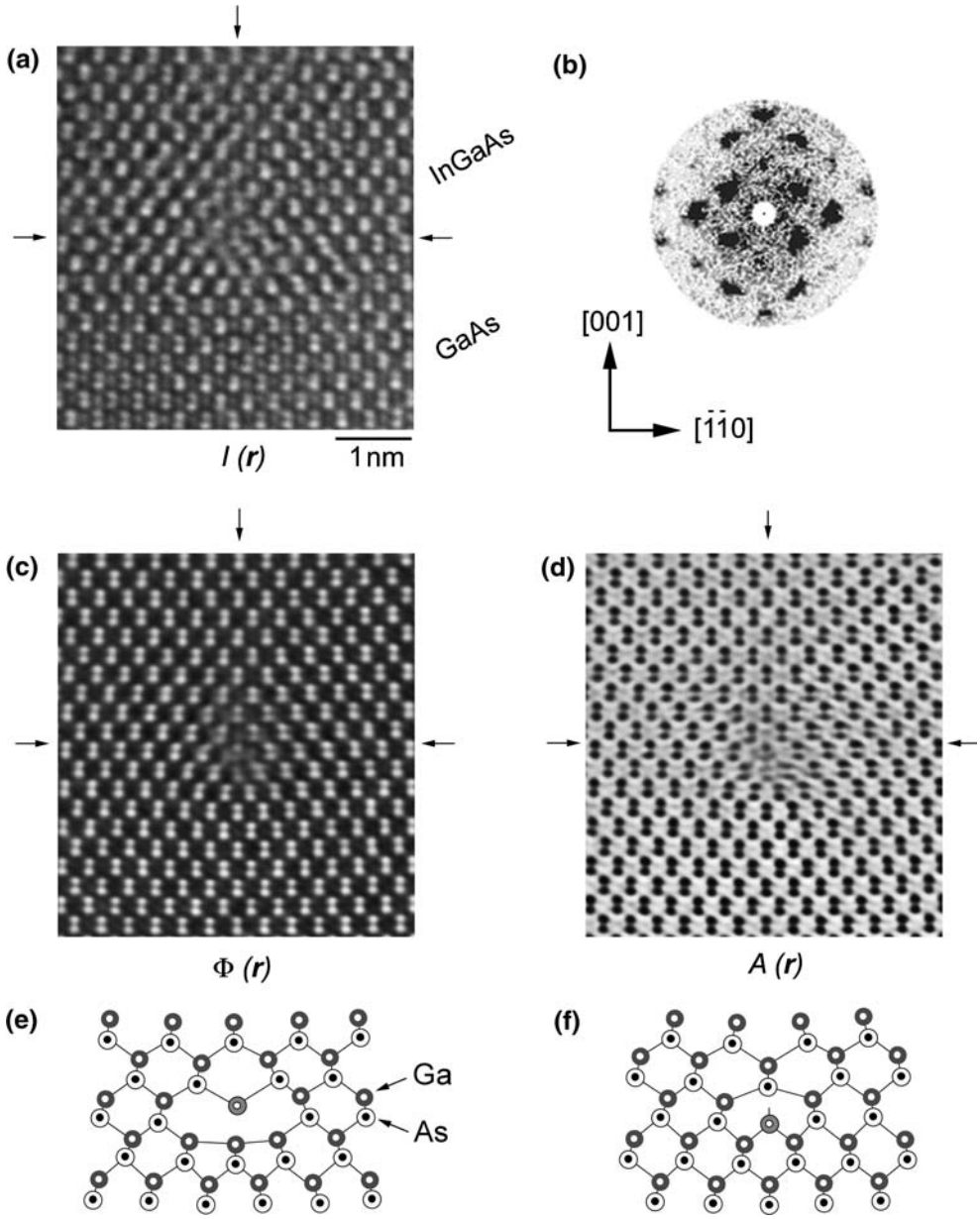

Fig. 4 Lomer-type edge dislocation with $\mathbf{b} = a/2\,[\bar{1}\bar{1}0]$ in the vicinity of an $In_{0.3}Ga_{0.7}As/GaAs$ heterointerface. (**a**) Optimum focus micrograph $I(\mathbf{r})$ taken along the $[1\bar{1}0]$ zone axis orientation of the sample. (**b**) ''Local'' diffraction pattern evaluated from the numerically restored exit-plane wavefunction of the image area. (**c**) Experimental phase image $\Phi(\mathbf{r})$ and (**d**) amplitude image $A(\mathbf{r})$ of the exit-plane wavefunction retrieved from a focal series of micrographs with the arrows indicating the dislocation core position. (**e**) Dislocation core model retrieved from the exit-plane wavefunction together with (**f**) the symmetrical glide set type core model as proposed by Hornstra [38]

single optimum focus micrograph $I(\mathbf{r})$ but only in the numerically retrieved amplitude and phase images displayed in Fig. 4c and d. Both $A(\mathbf{r})$ and $\Phi(\mathbf{r})$ show the atomic arrangement down to the dislocation core and reveal a detached atom column at the point of intersection of the extrapolated line positions indicated by the horizontal and vertical arrows added to the images. Relevant contrast features show mirror symmetry with respect to the medial $(\bar{1}\bar{1}0)$ lattice plane indicated by the upright arrows in the figure. This global symmetry behaviour ranges down to the dislocation core. In addition, the associated ''local'' diffraction pattern displayed in Fig. 4b, evaluated from the retrieved exit-plane wavefunction, reveals a proper zone axis orientation of the sample.

From both the $A(\mathbf{r})$ and the $\Phi(\mathbf{r})$ image a core structure model according to Fig. 4e can be directly deduced since contrast features may be interpreted intuitively. The dislocation core shows some similarity to the glide set type model of a Lomer dislocation originally proposed by Hornstra [38], which is displayed in Fig. 4f and characterized by an eight-atom inner ring. The present analysis, however, reveals a less compact core structure, which is built up of a ten-sided polygon also traversing the detached atom column with a coordination different from the surrounding matrix. This structure also deviates from the rather complex mirror symmetric dislocation cores observed at GaAs/Si interfaces [40, 41] and in Ge/Si heterosystems [42].

Referring to a more detailed discussion of the matter, it can be shown from a comparison of the optimum focus micrograph $I(\mathbf{r})$ with a variety of simulated images that the fundamental non-resolvability of the dislocation core is neither due to (i) the residual image delocalization, (ii) a locally decreased sample thickness, (iii) an immutably reduced occupancy of the atom columns during image recording or (iv) thin foil relaxation in the vicinity of the highly strained dislocation core [1]. Instead, the improved resolution of the phase $\Phi(\mathbf{r})$ and amplitude $A(\mathbf{r})$ images for practical applications results from the intrinsic averaging of structurally redundant information together with the electron-beam-induced time-dependent structural transformation of the sample, which is particularly pronounced close to the highly strained regions adjacent to the dislocation core. While numerical retrieval techniques adjust this information by averaging, a single Z_{opt} micrograph $I(\mathbf{r})$ in contrast only represents a snap-shot of a sample under illumination.

Materials science application: chromium implantation induced lattice defects in GaN (1120)

As a further example, we report on the atomic structure associated with partial dislocations introduced by chromium implantation into GaN layers. The implantation of transition metals into common semiconductor materials is regarded as a candidate process for the fabrication of diluted magnetic semiconductors [43]. A by-product of the implantation process is the creation of ion-induced lattice defects. Extrinsic and intrinsic basal plane stacking faults bound by Frank partial or Shockley-Frank partial dislocations are formed as a result of the precipitation of excess interstitials [28, 44].

The GaN layers presented in this study were grown by metal organic chemical vapour deposition on (0001) oriented sapphire substrates under Si doping to a concentration of 2×10^{17} cm^{-3}. Cr+ ions were implanted with an energy of 200 kV and a dose of 5×10^{16} cm^{-2} at a temperature of 350 °C to avoid amorphization in the as-implanted samples. A high density of basal plane stacking faults is observed besides spherical Cr-rich precipitates in the surface near regions after chromium implantation and rapid thermal annealing at 700 °C for 5 min in N_2 atmosphere [45].

The majority of the basal plane stacking faults are extrinsically bound by Frank partial dislocations with Burgers vectors of type $\mathbf{b} = 1/2$ [0001]. Figure 5 displays the amplitude image $A(\mathbf{r})$ and the phase image $\Phi(\mathbf{r})$ numerically retrieved from a through-focus series of micrographs of a perfect nanometre-sized interstitial loop close to the end of the range depth of implantation.

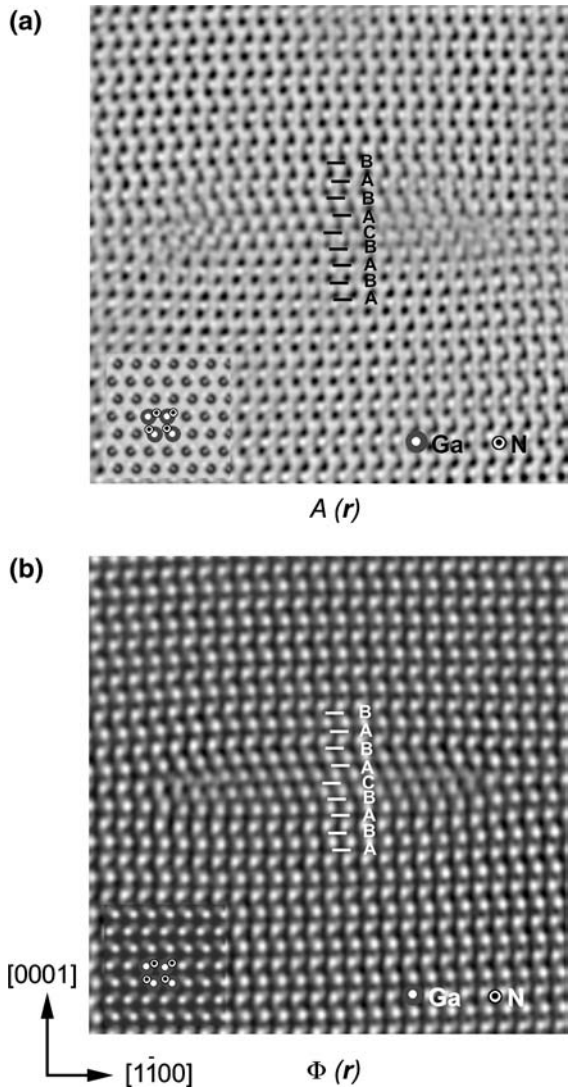

Fig. 5 Interstitial loop in Cr-implanted GaN viewed along the [11$\bar{2}$0] direction. (**a**) Amplitude image $A(\mathbf{r})$ and (**b**) phase image $\Phi(\mathbf{r})$ evaluated from a focal series of micrographs. Simulated images of the periodic N polarity GaN structure based upon the assumption of a sample thickness of 3.2 nm are superimposed in the lower left parts of the images. The stacking sequence is AB<u>ABCAB</u>AB, where the underlined part highlights sphalerite stacking

Gallium and nitrogen columns at a dumbbell distance of 0.114 nm, considerably smaller than the information limit of the instrument, are not fully resolved. Nonetheless, the N polarity of the sample is clearly visible from the directly interpretable bright contrast in the phase image. The tetrahedral coordination across the faulted layer stacking is confirmed, indicating that no foreign chromium-gallium alloy phase is connected with the planar defects.

A magnified view of the core of a Frank partial dislocation at the terminating zone of a dislocation loop of several 10 nm in size is shown in the Z_{opt} image and the

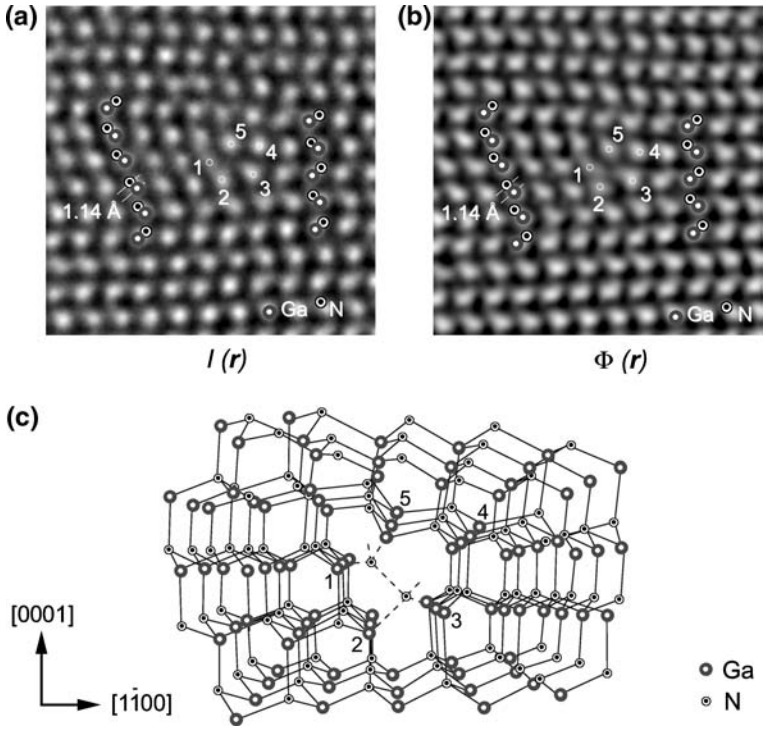

Fig. 6 Frank partial dislocation with a Burgers vector **b** = 1/2 [0001] projected along the 11$\bar{2}$0 direction. (**a**) Optimum focus micrograph $I(\mathbf{r})$ and (**b**) the corresponding phase image $\Phi(\mathbf{r})$ retrieved from the focal series of images together with (**c**) a stick and ball model of the 5/7 ring configuration for the core of the Frank partial dislocation

phase image $\Phi(\mathbf{r})$ retrieved from a corresponding focal series displayed in Fig. 6a and b, respectively. Although the Z_{opt} image $I(\mathbf{r})$ and the phase image $\Phi(\mathbf{r})$ appear quite similar at first glance, the improved signal-to-noise ratio in the phase image enhances the visibility of the nitrogen positions and the dumbbell orientation down to the core of the dislocation. The phase image $\Phi(\mathbf{r})$ strengthens the presence of further nitrogen atoms within the core surrounded by the cage of the five marked gallium columns. The faint phase shift in $\Phi(\mathbf{r})$, in which non-linear image components and image delocalization are eliminated, indicates a nitrogen-filled core in favour of a chromium- or gallium-rich core.

Based on these observations, a tentative 5/7 ring configuration for the core is presented in Fig. 6c. The nitrogen atoms shared by the 5- and 7-membered rings are coordinated threefold with Ga and N. Due to the wrong bond and the presence of unpaired electrons, this structure is not expected to be the most stable configuration. Since the phase image $\Phi(\mathbf{r})$ is retrieved from a through-focus series taken over a period of a few 10 s, the image conceivably reflects a transient state of the core that gathers further interstitials during observation. The Z_{opt} image level may therefore contain complementary but not necessarily identical information when compared to $\Phi(\mathbf{r})$. Indeed, in the present case the Z_{opt} image characterized by an inferior noise level compared to $\Phi(\mathbf{r})$ also supplies an alternative structure which contains two wrong Ga–Ga bonds connecting threefold-coordinated Ga atoms at positions 1–5 and 2–3, respectively.

Materials science application: grain boundaries in tantalum (001) thin films

Room-temperature magnetron sputter deposition of tantalum thin films on a multitude of crystalline and amorphous solid-state material substrates usually results in the formation of polycrystalline coatings with nanometre-sized crystallites [46, 47]. These crystallites mainly nucleate in a tetragonal β-phase and the material frequently undergoes a phase transformation towards a cubic α-phase at film thicknesses of about 10 to 20 nm [48, 49]. The metastable β-phase (space group $P4_2/mnm$), whose unit cell is displayed in Fig. 7 in two projections, shows atom column spacings as small as 0.127 nm when viewed along the crystallographic [001] direction.

The current technological interest in tantalum thin films is, however, primarily due to the ability of tantalum interlayers to promote the adhesion of copper to dielectrics [50] and because of good barrier properties against the diffusion of copper to silicon [51, 52]. As grain boundary diffusion in the polycrystalline films is admittedly supposed to become relevant at elevated temperatures [53] and molecular-dynamics simulations indicate a pronounced anisotropic migration behaviour of vacancies mediating the diffusion processes in β-Ta [54], the atomic-scale defect structure associated with the crystallites is, hence, the key to assessing the technological relevance of corresponding layers for thin film applications.

To analyse the atomic structure of grain boundaries in β-phase tantalum, thin films of nominal thickness

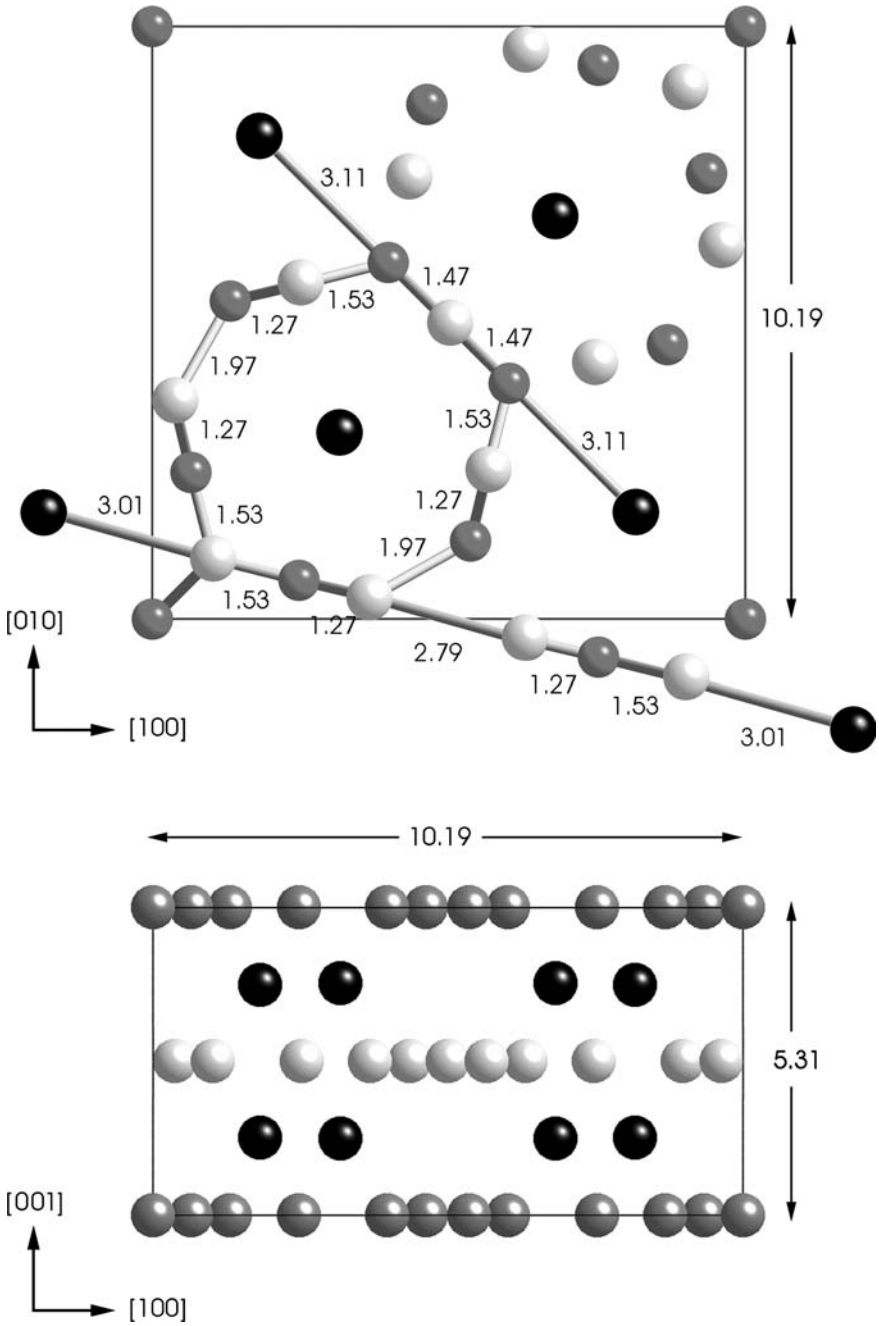

Fig. 7 Tetragonal β-tantalum unit cell ($P4_2/mnm$) viewed along the crystallographic [001] and [010] directions, respectively. The structure can be thought of as 22 atoms forming a pair of pseudo-hexagonal planes of different rotational orientation together with eight atoms lying halfway between these planes. In the figure, these pseudo-hexagonal planes are formed by the darker and lighter grey atoms located at positions $z = 0$ and $z = c/2$ along the [001] unit-cell axis, respectively, while black atoms lie in the intermediate planes at $z = c/4$ and $z = 3c/4$. When viewed along the [001] direction, the black atom positions represent doubly occupied columns with two atoms spaced one above the other per unit cell, whereas the greyish labelled columns are singly occupied. In this projection, the atoms belonging to the pseudo-hexagonal planes appear as septagons when connected by closed trajectories of straight lines. Each of these septagons encloses a doubly occupied tantalum column. The spacings indicated between adjacent atom columns represent projected distances given in ångström (0.1 nm) unit lengths

$d_{\mathrm{nom}} = 12$ nm were deposited on thin amorphous carbon support films (≈ 30 nm), which were suspended on standard copper grids. Deposition conditions were chosen as specified in a previous study and a combined ion-etching and plasma-cleaning procedure was applied for the removal of the carbon films and the preparation of electron transparent samples ensuring a sample thickness of less than 5 nm [3].

Figure 8 displays an experimental optimum focus micrograph $I(\mathbf{r})$ of a β-phase tantalum crystallite viewed along the [001] direction together with an amplitude image $A(\mathbf{r})$ numerically retrieved from the associated focal series of 15 micrographs. In the Z_{opt} image, a number of nearly detached contrast dots surrounded by irregular septagons are clearly visible with the latter being composed of twelve contrast dots of comparatively lower intensity. As can be seen from the comparison of the $I(\mathbf{r})$ micrograph with the calculated 2×2 unit-cell image insertion, both images coincide well if a specimen thickness of $t = 1.5$ nm is assumed and considering residual lens aberrations of $A_1 = 4.2$ nm (110°), $A_2 = 120$ nm (10°), and $B_2 = 70$ nm (340°) with the values in parentheses indicating azimuth

angles inclined with the horizontal image axis also representing the crystallographic [100] direction with respect to the simulations. Further instrumental parameters used for the calculations are identical to those specified in the previous sections.

When compared with the β-Ta structure projection displayed below the Z_{opt} image, it becomes evident that the central bright dot positions in the $I(\mathbf{r})$ micrograph are directly linked to the doubly occupied tantalum columns while the enclosing septagons cover the singly occupied columns appearing at comparatively decreased image intensity values. In the present case, negative spherical-aberration-corrected imaging performed under optimized conditions thus not only results in bright atom contrast but in a sense represents an occupancy-sensitive imaging mode.

However, minor contrast pattern asymmetries, such as the elliptical distortion of the central contrast dots and the increased blurring of the septagon-related contrast feature along the [15 4 0] direction compared to the orthogonal [$\bar{4}$150] direction, only coincide when the above-specified parasitic lens aberrations are properly considered in the numerical simulations. Since contrast patterns calculated assuming reasonable crystal misorientations and specimen thicknesses are essentially different from that of the Z_{opt} micrograph, the residual lens aberrations are indeed the most striking potential sources of these elliptical image distortions and the anisotropic blurring of certain contrast features [3]. This finding only demonstrates once more that proper control of the residual aberrations and an improved long-term stability of the instrumental set-up will play a key role when operating future generation microscopes at the verge of the information limit.

Whereas $I(\mathbf{r})$ shows slightly smeared intensity peaks at the tantalum columns, the retrieved $A(\mathbf{r})$ image demonstrates clearly separated and distinctly decreased amplitude minima at these positions. The experimental $A(\mathbf{r})$ image coincides well with the calculated insertion, but is again characterized by an inferior signal-to-noise ratio when compared to the calculated images. Associated line profiles $A(x)$ extracted from the amplitude image $A(\mathbf{r})$ and measured along the crystallographic x = [15$\bar{4}$0] and x = [1$\bar{1}$0] directions are displayed in Fig. 9. The profile positions with respect to the $A(\mathbf{r})$ image are drawn as two pairs of lighter (experimental) and darker grey (calculated) arrows in Fig. 8 each indicating the above-mentioned crystallographic directions in β-phase tantalum viewed along the [001] zone axis. In the evaluation, the profiles are averaged perpendicular to the line direction over a width of 0.039 nm to improve the signal-to-noise ratio.

In general, paired profiles $A_{exp}(x)$ and $A_{sim}(x)$ are in fair agreement on a relative level although absolute amplitude values and profiles shapes are not in precise agreement.

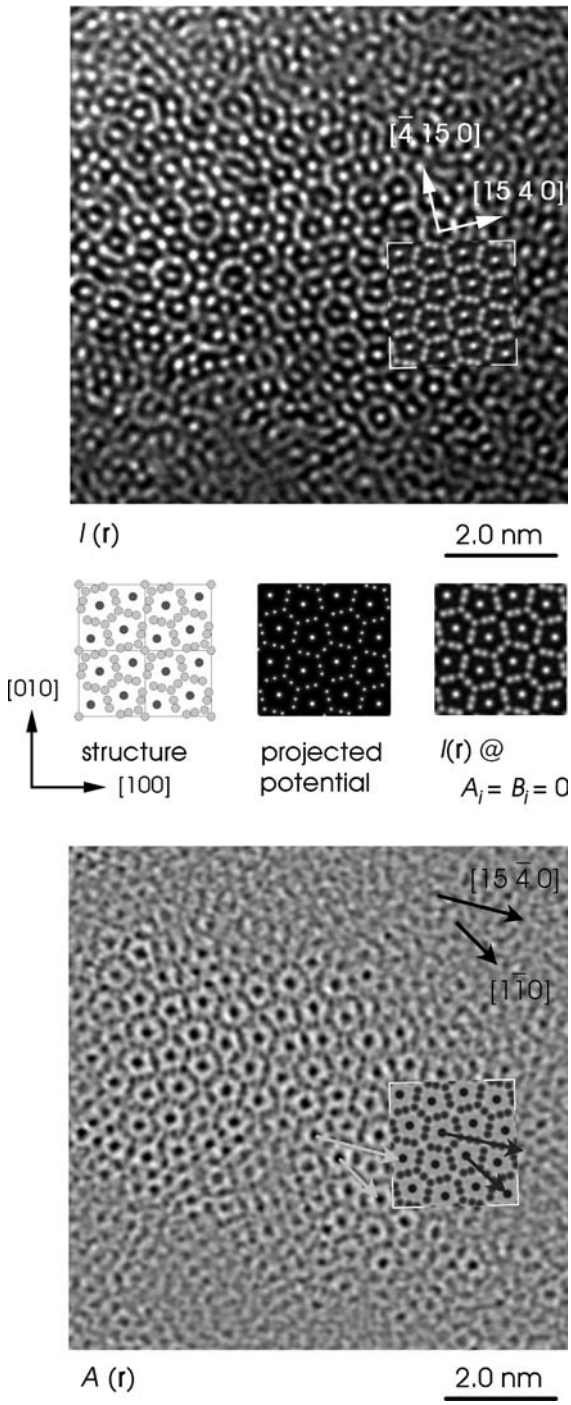

Fig. 8 Extended β-phase tantalum crystallite viewed along the [001] zone axis. Optimum focus micrograph $I(\mathbf{r})$ with the 2×2 unit cell showing a calculated image assuming t = 1.5 nm, Z = 11.6 nm, A_1 = 4.2 nm (110°), B_2 = 70 nm (340°) and A_2 = 120 nm (0°) as simulation parameters. The three images below the micrograph display the corresponding structure model together with the projected potential map and a calculated image assuming $A_1 = B_2 = A_2 = 0$ at otherwise fixed calculation parameters. Experimental amplitude image $A(\mathbf{r})$ evaluated from a focal series of 15 micrographs. The two pairs of lighter and darker grey arrows along the [1540] and [1$\bar{1}$0] directions indicate positions at which intensity line profiles displayed in Fig. 9 have been extracted from the experimental and simulated $A(\mathbf{r})$ images, respectively

This is especially true in view of a lateral narrowing of high amplitude plateau areas, which appear more peaked in the experimental profiles, cf. the shapes between the outermost doubly-occupied tantalum columns positions. In other words, the different steepness of profiles $A_{\mathrm{exp}}(x)$ and $A_{\mathrm{sim}}(x)$ reveals that the simulated profiles are characterized by a slightly higher resolution compared to the experimental data. This observation may be due either to vibrations of the sample or the residual image delocalization of $R \approx 0.08$ nm still present in spherical aberration-corrected microscopy [15] but also because of the well-known factor-of-three difference in image contrast between experimental and simulated images [55, 56].

Numerical values on column spacings Δx_{exp} and Δx_{sim} as measured from the extrema positions in the $A_{\mathrm{exp}}(x)$ and $A_{\mathrm{sim}}(x)$ profiles, respectively, are specified in the centre of Fig. 9. Specified error values represent uncertainty intervals due to the discretization of the corresponding images. Measured column spacing Δx_{exp} and Δx_{si} coincide to a large extent and, thus, confirm a point-to-point resolution of at least 0.13 nm at directly interpretable amplitude images.

When compared to the singly occupied tantalum columns, distinctly decreased amplitude values are observed in all profiles at the doubly occupied columns. This observation is directly linked to the increased projected scattering potential and may be interpreted as a kind of occupancy-sensitive imaging mode. The generalization of this observation towards arbitrary diffraction conditions or even for quantification purpose is, however, far from straightforward since conspicuous image artefacts, e.g. wrap-around effects, are observed at increased specimen thicknesses.

Due to the atomic-resolution capabilities of the analysis technique, we may finally discuss some aspects of the defect structure and the mechanisms of crystallite growth related to materials science. In Fig. 10, the singly occupied tantalum columns are superimposed onto the $A(\mathbf{r})$ image together with individual [001] unit-cell edgings. The associated network reveals the crystallite to be composed of four grains, which are highlighted by different grey levels and are rotated against each other by variable multiples of approximately 30° thus proving the existence of asymmetric 30° tilt grain boundaries of the type:

$$(001)_{\kappa}||(001)_{\varphi} \text{ and } [010]_{\kappa}||[\bar{1}\sqrt{3}0]_{\varphi} \tag{7}$$

with κ and ϕ denoting neighbouring grains. In spite of the uniform 30° tilt properties, a common uniform habitat plane cannot be assigned to all of the four boundaries. Most boundary segments are found to run along directions, which satisfy the principle that the atom columns in the adjoining grains have closely similar patterns and spacings at the common boundary. Main boundary segment directions cover the crystallographic <100> and <110> directions. No larger amorphous areas between adjacent grains are observed.

The nearly precisely 30° rotational relationships between adjacent grains and the absence of amorphous zones between these grains allows some insights with respect to the nucleation process of the crystallite. As it is

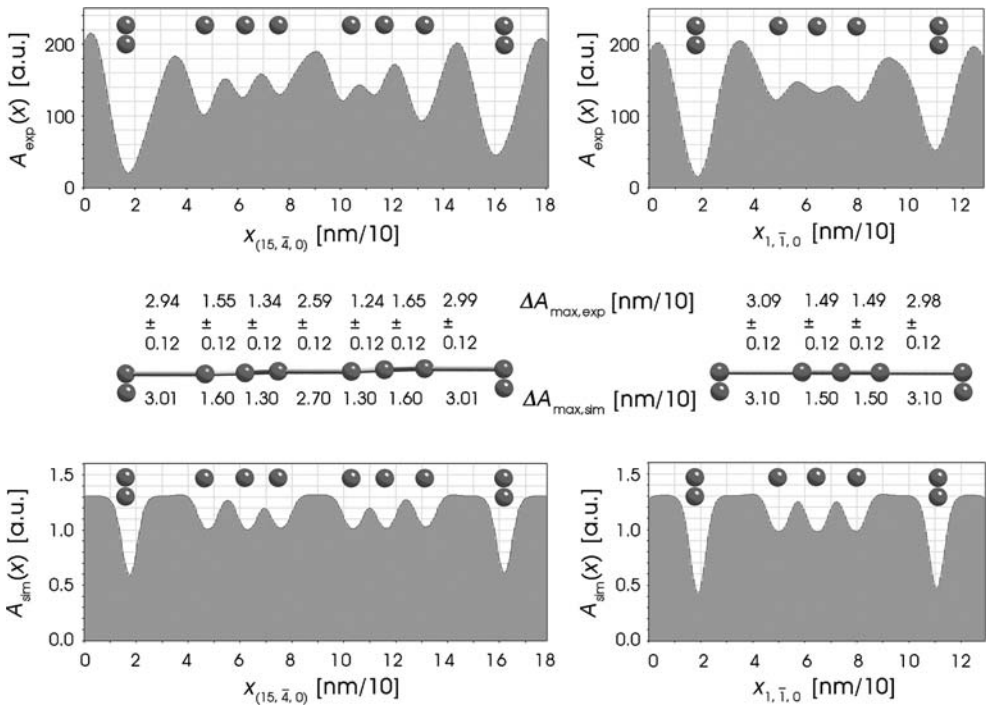

Fig. 9 Amplitude line profiles $A_{\mathrm{exp}}(x)$ and $A_{\mathrm{sim}}(x)$ extracted from the experimental and simulated areas of the $A(\mathbf{r})$ image displayed in Fig. 8, respectively. The profiles cover the crystallographic [15$\bar{4}$0] and [1$\bar{1}$0] directions. In each profile, the number of atoms drawn in at the amplitude extrema positions indicates the occupancy of the corresponding column. Numerical data on spacings Δx_{exp} and Δx_{sim} between adjacent amplitude minima positions have been extracted from the displayed $A_{\mathrm{exp}}(x)$ and $A_{\mathrm{sim}}(x)$ profiles

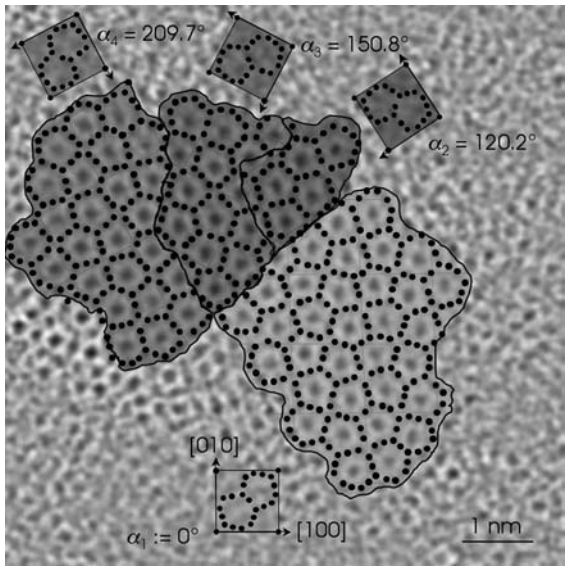

Fig. 10 Amplitude image $A(\mathbf{r})$ according to Fig. 8 with the positions of the singly occupied tantalum columns superimposed (•) and the borders of the unit cells indicated by faint grey squares. The crystallite as a whole is found to be composed of four grains highlighted by different grey levels rotated against each other by multiples of 30°

quite unlikely that all four grains will have already started growing with the observed rotational orientation on an amorphous substrate and since a spontaneous rotational re-alignment of monolithic grains by means of an integrative *ad hoc* rotation immediately before they coalescence would require a dedicated activation energy [57] both of these potential mechanisms may be ruled as being fairly improbable.

Instead, a more reasonable explanation would be that the 30° tilt boundaries are directly grown-in at the free surfaces of a single laterally expanding grain, which involves the adsorption of tantalum atoms at misaligned unit-cell positions. Due to a certain amount of energy transfer from impinging atoms these processes may even take place during room temperature sputtering of metal systems [58]. The direct grain-boundary formation during adsorption is also corroborated by the observed mirror-symmetric habit planes and the absence of twist components between all four grains and, especially, by the absence of thin amorphous interspacings between adjacent grains.

Conclusions

A combined approach involving negative spherical aberration imaging in tandem with the numerical retrieval of the exit-plane wavefunction was applied to the investigation of dislocation core structures and grain boundaries in common semiconductor materials and metastable metallic phases at atomic resolution. It was demonstrated that recent improvements in the resolving power of aberration-corrected transmission electron microscopes enable the imaging of very fine structure details with column spacings well below 0.13 nm at directly interpretable contrast features associated with an extensively minimized image delocalization when micrographs are taken under directly interpretable bright-atom contrast conditions by applying a $C_S < 0$ set-up of the instrument and an optimum defocus $Z_{opt} > 0$. This imaging mode thus allows a largely direct interpretation of experimental images down to the information limit of the instrument.

Additionally, the numerical retrieval of the exit-plane wavefunction was shown to be a most suitable tool for the measurement and subsequent elimination of residual lens aberrations still present in aberration-corrected high-resolution microscopy. By this means, artificial contrast features still visible in micrographs taken under optimized imaging conditions could be successfully eliminated, which is especially beneficial when investigating the structure of lattice defects and heterointerfaces at atomic resolution. Apart from this specific purpose, the numerical restoration of the exit-plane wavefunction was demonstrated to be an appropriate implement for the recognition and on-line correction of minor sample misalignments during operation of the electron microscope.

Apart from these individual advantages, both techniques dramatically improve the accurate identification of lattice imperfections in semiconductor materials at hitherto unequalled imaging quality when employed in combination. Experimental analyses benefit conspicuously from an increase of the instrumental resolution together with the pre-reduction of lens aberrations by hardware correction as well as from the complete elimination of residual aberrations by the numerical retrieval of the exit-plane wavefunction, which is also free from non-linear imaging artefacts and yields images characterized by an improved signal-to-noise ratio.

For exemplification purposes, the atomic core structure of Lomer dislocation in the vicinity of $In_{0.3}Ga_{0.7}As/GaAs$ heterointerfaces was reviewed and directly identified as being composed of a mirror symmetric 10-atom ring thus rendering extensive image simulations superfluous. Local lattice distortions associated with partial dislocations terminating extrinsic stacking faults in GaAs were quantified by means of the analysis of experimental phase images $\Phi(\mathbf{r})$ providing clear evidence of the set-up of the terminating dislocation core structure. A similar quantitative analysis focusing on lattice imperfections in GaN based on the synergetic combination of negative spherical aberration-corrected imaging and the numerical retrieval of the exit-plane wavefunction is presently hampered by the limited resolution of the instrument used in this study, but

will find practical application with the new generation of aberration-corrected microscopes with sub-ångström resolution capabilities. Finally, the largely minimized image delocalization also permitted the identification of asymmetric 30° tilt boundaries between β-phase tantalum grains, which were found to be devoid of any amorphous areas in between adjacent grains.

Acknowledgements The authors are grateful to Arno Förster, Vitaly Guzenko, Martin Weides and Doris Meertens for making available the samples investigated in this compilation and for painstaking specimen preparation work.

References

1. Tillmann K, Thust A, Urban K (2004) Microsc Microanal 10:185
2. Tillmann K, Houben L, Thust A (2006) Phil Mag (in press)
3. Tillmann K, Thust A, Gerber A, Weides MP, Urban K (2005) Microsc Microanal 11:534
4. Kisielowski C, Hetherington CJD, Wang YC, Kilaas R, O'Keefe MA, Thust A (2001) Ultramicroscopy 89:243
5. O'Keefe MA, Nelson EC, Wang EC, Thust A (2001) Phil Mag B 71:1861
6. Freitag B, Kujawa S, Mul PM, Ringnalda J, Tiemeijer PC (2005) Ultramicroscopy 102:209
7. Jia CL, Lentzen M, Urban K (2003) Science 299:870
8. Jia CL, Lentzen M, Urban K (2004) Microsc Microanal 10:174
9. Hutchison JL, Titchmarsh JM, Cockayne DJH, Doole RC, Hetherington CJD, Kirkand AI, Sawada H (2005) Ultramicroscopy 103:7
10. Lichte H (1991) Ultramicroscopy 38:13
11. Coene W, Jansen AJEM (1992) Scan Microsc Suppl 6:379
12. Rose H (1990) Optik 85:19
13. Haider M, Rose H, Uhlemann S, Schwan E, Kabius B, Urban K (1998) Nature 392:768
14. Kujawa S, Freitag B, Hubert D (2005) Microsc Today 13(4):16
15. Lentzen M, Jahnen B, Jia CL, Thust A, Tillmann K, Urban K (2002) Ultramicroscopy 92:233
16. Coene WMJ, Janssen G, Op de Beeck M, van Dyck D (1992) Phys Rev Lett 69:3743
17. Coene WMJ, Thust A, Op de Beeck M, van Dyck D (1996) Ultramicroscopy 64:109
18. Thust A, Coene WMJ, Op de Beeck M, van Dyck D (1996) Ultramicroscopy 64:211
19. Thust A, Overwijk MHF, Coene WMJ, Lentzen M (1996) Ultramicroscopy 64:249
20. Thust A, Jia CL, Urban K (2002) In: Cross R (ed) Proceedings ICEM-15, vol 1. Microscopy Society of Southern Africa, Durban, pp 167–168
21. Williams DB, Carter CB (1996) Transmission electron microscopy. Plenum Press, New York (U.S.) and London (U.K.)
22. Lentzen M (2004) Ultramicroscopy 99:211
23. O'Keefe MA, Hetherington CJD, Wang YC, Nelson EC, Turner JH, Kisielowski C, Malm JO, Mueller R, Ringnalda J, Pan M, Thust A (2001) Ultramicroscopy 89:215
24. Chang LY, Chen FR, Kirkland AI, Kai JJ (2003) J Electron Microsc 52:359
25. Houben L, Thust A, Urban K (2006) Ultramicroscopy 106:200
26. Uhlemann S, Haider M (1998) Ultramicroscopy 72:109
27. Zemlin F, Weiss K, Schiske P, Kunath W, Herrmann KH (1978) Ultramicroscopy 3:49
28. Hirth JP, Lothe J (1968) Theory of dislocations. McGraw-Hill, New York (U.S.)
29. Amelinckx S (1979) In: Nabarro FRN (ed) Dislocations in solids, vol 2. North-Holland, Amsterdam, pp 67–460
30. Nunes RW, Bennetto J, Vanderbilt D (1998) Phys Rev B 58:12563
31. Justo JF, Nunes RW, Assali LVC (2002) J Phys: Condens Matter 14:12749
32. Beckman SP, Xu X, Specht P, Weber ER, Kisielowski C, Chrzan DC (2002) J Phys: Condens Matter 14:12673
33. Kolar HR, Spence JCH, Alexander H (1996) Phys Rev Lett 77:4031
34. Xu X, Beckmann SP, Specht P, Weber ER, Chrzan DC, Ernie RP, Arslan I, Browning N, Bleloch A, Kisielowski C (2005) Phys Rev Lett 95:145501
35. Hÿtch MJ, Snoeck E, Kilaas R (1998) Ultramicroscopy 74:131
36. Gomez AM, Hirsch PB (1978) Phil Mag A 38:733
37. Lomer WM (1951) Phil Mag 42:1327
38. Hornstra J (1958) J Phys Chem Solids 5:129
39. Bourret A, Dessaux J, Renault R (1982) Phil Mag A 45:1
40. Vilà A, Cornet A, Morante JR, Ruterna P, Loubradou M, Bonnet R, González Y, González L (1995) Phil Mag A 75:85
41. Lopatin S, Pennycook SJ, Narayan J, Duscher G (2002) Appl Phys Lett 81:2728
42. Stirman JN, Crozier PA, Smith DJ, Phillipp F, Brill G, Sivananthan S (2004) Appl Phys Lett 84:2530
43. Ohno H (1998) Science 281:951
44. Kirchner V, Heinke H, Birkle U, Einfeld S, Selke D, Ryder PL (1998) Phys Rev B 58:15749
45. Guzenko VA, Thillosen N, Dahmen A, Calarco R, Schäpers Th, Houben L, Luysberg M, Schineller B, Heuken M, Kaluza A (2004) J Appl Phys 96:5663
46. Westwood WD, Waterhouse N, Wilcox PS (1975) Tantalum thin films. Academic Press, London (U.K.)
47. Hieber K, Mayer NM (1982) Thin Solid Films 90:43
48. Read MH, Altman C (1965) Appl Phys Lett 7:51
49. Moseley PT, Seabrook CJ (1973) Acta Cryst B29:1170
50. Kwon KW, Lee HJ, Sinclair R (1999) Appl Phys Lett 75:935
51. Laurila T, Zeng K, Kivilahti K, Molarius J, Suni I (2000) J Appl Phys 88:3377
52. Hübner R, Hecker M, Mattern N, Hoffmann V, Wetzig K, Wenger C, Engelmann HJ, Wenzel C, Zschech E, Bartha JW (2003) Thin Solid Films 437:248
53. Gupta D (1995) Mater Chem Phys 41:199
54. Klaver P, Thijsse B (2002) Thin Solid Films 413:110
55. Hÿtch MJ, Stobbs WM (1994) Ultramicroscopy 53:191
56. Boothroyd CB (1998) J Microsc 190:99
57. Venables JA, Spiller GDT, Hanbücken M (1984) Rep Prog Phys 47:399
58. Abelmann L, Lodder C (1997) Thin Solid Films 305:1